

Deep Generative Modeling with Spatial and Network Images: An Explainable AI (XAI) Approach

Yeseul Jeon^{1,2}, Rajarshi Guhaniyogi^{1,†}, Aaron Wolfe Scheffler^{2,†}

¹Department of Statistics, Texas A&M University, College Station, TX, USA

²Department of Epidemiology & Biostatistics, University of California San Francisco, San Francisco, CA, USA.

† These authors have contributed equally to this work.

Abstract

This article addresses the challenge of modeling the amplitude of spatially indexed low frequency fluctuations (ALFF) in resting state functional MRI as a function of cortical structural features and a multi-task coactivation network in the Adolescent Brain Cognitive Development (ABCD) Study. It proposes a generative model that integrates effects of spatially-varying inputs and a network-valued input using deep neural networks to capture complex non-linear and spatial associations with the outcome. The method models spatial smoothness, accounts for subject heterogeneity and complex associations between network and spatial images at different scales, enables accurate inference of each images effect on the outcome image, and allows prediction and inference with uncertainty quantification via Monte Carlo dropout, contributing to one of the first Explainable AI (XAI) frameworks for image-on-image regression with spatial and network images. The model is highly scalable to high-resolution data without the heavy pre-processing or summarization often required by Bayesian methods. We applied the XAI model to the ABCD data which revealed associations between cortical features and ALFF throughout the entire brain. Our model performed comparably

or a bit better than existing methods in predictive accuracy but provided superior uncertainty quantification and faster computation, demonstrating its effectiveness for large-scale neuroimaging analysis. A supplementary file contains additional simulation results and additional results from the ABCD data analysis.

Keywords: Deep neural network; explainable artificial intelligence; Monte Carlo (MC) dropout; multimodal neuroimaging data; variational inference; uncertainty quantification.

1 Introduction

Recently, a critical concern in the field of neuroimaging has been unraveling the intricate relationships between images that capture different aspects of brain structures and function using magnetic resonance imaging (MRI). This involves integrating multimodal imaging data—specifically, (a) *brain network information* from functional MRI (fMRI), which quantifies connectivity between nodes, and (b) *brain spatial information* from structural MRI (sMRI) and fMRI, which offers ROI-level information. These data are hierarchically structured, with ROIs nested within network nodes, offering insights at multiple scales.

For example, this article is motivated by the challenge of modeling the amplitude of spatially indexed low-frequency fluctuations (ALFF) in resting state functional MRI (rs-fMRI) as a function of cortical structural features measured via sMRI and a multi-task coactivation network capturing coordinated patterns of brain activation measured via task-based fMRI (t-fMRI) in a large neuroimaging study of adolescents. Recent studies in cognitive neuroscience suggest that ALFF serves as an indicator of brain functional integrity and supports information processing [Fu et al., 2017]. It has been linked to atypical cognitive development, cognitive decline, and various psychiatric disorders, highlighting its relevance for both basic and clinical neuroscience research [Sheng et al., 2021]. What remains unclear from current research is how spatial and network features of the brain contribute jointly to explain variability in ALFF. A major challenge in bridging this gap is a lack of available methods that can accommodate heterogeneity in multimodal imaging data and the immense data volume

produced in large neuroimaging studies while simultaneously providing principled inference.

The primary scientific objectives of this study encompass whole-brain analysis and are threefold: (a) to predict the spatially indexed ALFF outcome using both cortical structural predictors and a brain network predictor; (b) to jointly model the spatially varying effects of the structural predictors on ALFF through interpretable regression functions, enabling inference on the contributions of cortical features; and (c) to quantify uncertainty in model components and predictions, facilitating principled statistical inference. These scientific goals must be met while accommodating the data volume produced from large neuroimaging studies required to detect the often-subtle effects that link brain image features.

To achieve these goals, this article proposes a two-stage generative model for input and outcome images. In the first stage, each edge of the network predictor is modeled as an interaction between latent vectors associated with the nodes, enabling the estimation of node-specific latent effects. The second stage adopts a semi-parametric regression approach that incorporates additive contributions from both spatial and network predictors. Spatial effects are captured using nonlinear spatially varying coefficient functions, while the influence of each network node is modeled as a function of the latent effects estimated in the first stage.

These nonlinear functions are modeled using deep neural networks (DNNs) with a dropout architecture. To perform inference, we employ *Monte Carlo dropout* (MC dropout) architecture [Gal and Ghahramani, 2016b], leveraging its connection to deep Gaussian processes (GP). This allows us to predict the output image and to estimate the regression effects of spatial predictors and nonlinear node effects, all with quantified uncertainty, offering one of the first *explainable AI* methods in the context of heterogeneous image-on-image regression.

1.1 Novelty of the Proposed Approach

(1) Integration of multimodal data for image prediction. The proposed framework seamlessly integrates spatial and network images across multiple scales, leveraging their structural relationships through a flexible, nonlinear, multiscale modeling approach to enable predictive inference for an outcome image. Image-on-image regression exploiting the

structures of both spatial and network inputs and their nonlinear effects jointly on spatial outputs remains largely underexplored, making this one of the first principled methods to address the problem. **(2) Explainable inference.** Our approach leverages the connection between deep Gaussian processes and dropout-based deep neural networks (DNNs) to generate approximate posterior samples of DNN parameters. This approach leads to both point estimation and uncertainty quantification for the effects of spatial predictors and network nodes, as well as for the predicted outcome image. This enables interpretable inference and positions our method as one of the *first deep learning-based* frameworks to offer explainability in image-on-image regression. **(3) Computational efficiency.** The model is highly scalable, with computation growing linearly in both the sample size and the number of ROIs, enabling its future use in larger neuroimaging studies. **(4) State-of-the-art performance.** Empirical results demonstrate that our approach achieves competitive point estimates and predictions while substantially outperforming existing methods in uncertainty quantification.

1.2 Related Work

Image datasets represent high-dimensional, structured data characterized by complex dependency patterns. To model these intricacies, many studies have leveraged deep learning architectures capable of capturing nonlinear dependencies through multiple layers of parameterization [Tsuneki, 2022, Razzak et al., 2018]. Bayesian deep learning frameworks are especially attractive for their flexibility of offering coherent probabilistic inference. Bayesian methods are increasingly applied in medical imaging for tasks like classification, segmentation, and tumor growth prediction [Zou et al., 2023, Prince et al., 2023, Jeon et al., 2024]. However, deep learning approaches for predictive inference of outcome images based on input images, popularly referred to as the image-on-image regression, remain notably limited.

Several recent studies align with our framework by incorporating spatial information into Bayesian deep learning [Kirkwood et al., 2022, Li et al., 2023, Zammit-Mangion et al., 2023, Mateu and Jalilian, 2022]. For example, Mateu and Jalilian [2022] used variational autoencoder-based generative networks for spatio-temporal point processes, while Kirkwood

et al. [2022] applied Bayesian deep neural networks to spatial interpolation. Li et al. [2023] proposed replacing splines or kernels with DNNs to model nonlinear spatial variation in semiparametric regression. Spatial Bayesian neural networks (SBNNs) [Zammit-Mangion et al., 2023] enhance flexibility by incorporating spatial embeddings and spatially varying parameters within BNNs, though at higher computational cost. Unlike our method, which directly models spatially varying coefficients, SBNNs rely on spatial basis functions and learn weight and bias parameters in neural networks via embedding layers.

For interpretable machine learning in the context of image-on-image regression, one of the most relevant methods is BIRD-GP [Ma et al., 2023]—a two-stage Bayesian model that employs a combination of GPs and DNNs. Specifically, this approach uses neural networks to learn basis expansions of input and output images, followed by nonlinear regression on vectorized projections of the input and output images. While BIRD-GP provides predictive uncertainty through the posterior distribution, its two-stage design may lead to increased computational cost and a greater risk of overfitting. The proposed approach offers competitive inference to BIRD-GP in all empirical investigation and is much faster in computation.

The remainder of the paper is structured as follows. Section 2 describes the ABCD neuroimaging dataset and outlines the associated scientific objectives. Section 3 presents the proposed methodology and explains how the framework enables interpretable inference using DNNs. Section 5 assesses performance through simulation studies, followed by an application to the ABCD data in Section 6. Section 7 concludes with a discussion. Additional results on simulations and ABCD data can be found in the supplementary file.

2 Imaging Data from the ABCD Study

This article explores a clinical application involving multimodal imaging data from Adolescent Brain Cognitive Development (ABCD) Study [Casey et al., 2018]. The primary aim is to investigate how spatial variability in rs-fMRI signals across time, reflecting the amplitude of low frequency oscillations, relates to both spatial brain characteristics and a multi-task

brain coactivation network. We begin by introducing motivating scientific question.

2.1 Motivating Scientific Question

fMRI captures blood-oxygen-level dependent (BOLD) signals in the brain while subjects are at rest or engaged in tasks, enabling the assessment of localized neuronal activity. Fluctuations in the BOLD signal across time—typically quantified through variance or standard deviation of the time series—are now increasingly viewed as meaningful indicators of brain function rather than random noise, and are interpreted as reflecting the amplitude of low-frequency fluctuations (ALFF) defined as the power of the BOLD signal between 0.01 and 0.10 Hz [Zuo et al., 2010, Hagler Jr et al., 2019, Wang et al., 2021]. Existing studies have linked ALFF with structural properties of the brain via diffusion MRI (dMRI) [Wang et al., 2021]; gray and white matter content assessed through structural MRI (sMRI) [Zuo et al., 2010]), patterns of functional connectivity in brain networks (rs-fMRI [Fu et al., 2017, Sheng et al., 2021, Tomasi et al., 2016]), and response to task performance (task-based fMRI (t-fMRI) [Tomasi and Volkow, 2019]).

Building on this evidence, emerging findings in both computational and cognitive neuroscience suggest that ALFF serves as a marker of functional brain integrity, supports core processes of long distance information handling, and changes in response to task-activation [Zuo et al., 2010, Tomasi and Volkow, 2019]. The association of ALFF with both resting state networks and task-based brain activation is reinforced by the growing acceptance that resting state brain networks are associated with task-based activation and functional integration [Cole et al., 2016, Ye et al., 2022]. What is unclear from current work is how structural and network characteristics of the brain jointly contribute variation in observed ALFF. Specifically, we are interested in modeling ALFF as a function of brain structure (cortical thickness and gray-white matter intensity contrasts measured via sMRI) and a multi-task coactivation network capturing coordinated patterns of brain activation during the execution of several cognitive tasks (measured via t-fMRI). In modeling variation in ALFF from multiple images, it is desirable to provide interpretable mappings of each input image onto the outcome as

well as principled uncertainty quantification in terms of model components and prediction.

Most statistical modeling of ALFF to date has concentrated on linking BOLD signal variability or ALFF distributions to either structural or functional brain characteristics by extracting targeted predictor variables from a *single* imaging modality and applying relatively straightforward statistical techniques. These investigations have included t-test comparisons of ALFF across regions dominated by gray versus white matter [Zuo et al., 2010], regional modeling of ALFF as a function of global white matter maturation through linear mixed effects models [Wang et al., 2021], linear regression modeling to associate ALFF with task-based activation maps [Tomasi and Volkow, 2019], and studies connecting ALFF to resting-state connectivity using parametric mapping and correlational analyses of various functional graph metrics [Sheng et al., 2021, Tomasi et al., 2016]. Recently, source localization has been used to associate low-frequency fluctuations captured by magnetoencephalography with ALFF derived from fMRI [Zhang et al., 2023]. However, no study has jointly modeled ALFF using both structural and network images, despite growing evidence that these modalities provide complementary information [Sui et al., 2012].

2.2 Clinical Imaging

We used data from the ABCD Study 5.0 Tabulated Release (<http://dx.doi.org/10.15154/8873-zj65>), focusing on baseline imaging measures from children aged 9–10 years. Imaging data were acquired and processed as outlined in Hagler Jr et al. [2019]. All images were aligned to the Montreal Neurological Institute (MNI) template space and parcellated to the Destrieux atlas (Figure 1(a); [Destrieux et al., 2010]) yielding 148 spatially defined regions of interests (ROIs) grouped into 12 nodes defined by brain hemisphere (left, right) and lobe (frontal, parietal, occipital, insula, and limbic). Thus, the data has hierarchical structure in which ROIs are organized within a collection of mutually exclusive nodes. Our outcome measure is the variance of the BOLD signal measured via rs-fMRI (BOLDVAR; Figure 1(b)) at each ROI which is considered a proxy for ALFF [Hagler Jr et al., 2019] and is log transformed to better satisfy model assumptions in Section 3. We consider two structural cortical pre-

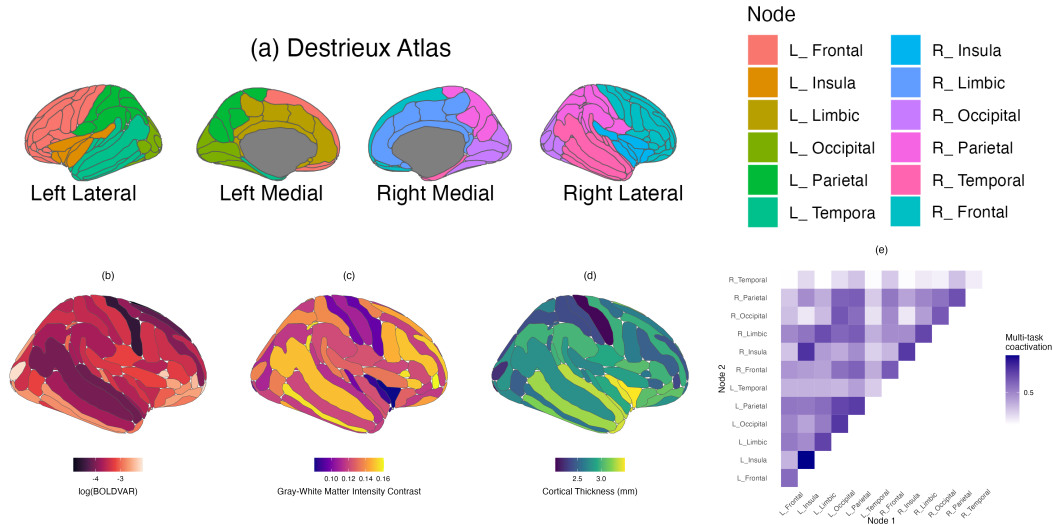


Figure 1: (a) The Destrieux atlas used to parcellate our motivating ABCD imaging data into 148 ROIs grouped by nodes defined by hemisphere (left, right) and lobes (frontal, parietal, occipital, insula, and limbic). (b) Outcome of interest: variance in the rs-fMRI BOLD time series (BOLDVAR) which is a proxy for amplitude of low frequency fluctuations (ALFF). (c) Structural predictor: cortical gray/white matter intensity contrast (GWMIC). (d) Structural predictor: cortical thickness (CT). (e) Network predictor: multi-task coactivation matrix representing brain coactivation across 12 nodes in response to an array of cognitive tasks.

dictors measured via sMRI at each ROI: cortical gray and white matter intensity contrasts (GWMIC; Figure 1(c)), thought to capture brain development, and cortical thickness (CT; Figure 1(d)), a local measure of gray matter thickness. We also consider a network image predictor which captures multi-task brain coactivation (Figure 1(e)), a measure of coordinated neuronal activation across the brain while performing different tasks. Specifically, we obtained task-activation maps measuring local BOLD signals via t-fMRI collected on subjects while engaged in three tasks (money incentive delay task, stop signal task, and emotional version of the n-back task) with four contrasts per task yielding twelve task-activation maps as described in Ye et al. [2022]. Based on the twelve task-activation maps, we constructed a correlation matrix among ROIs in the brain for each subject which we then averaged by node to yield a 12×12 multi-task coactivation matrix representing patterns of brain coactivation across hemispheres and lobes in response to a diverse array of tasks. Our aim is to expand the investigation of ALFF by integrating multimodal image inputs to better understand how

structural and network-level factors together influence local variability in rs-fMRI signals. To address this, we introduce novel regression framework, as outlined in Section 3.

3 Methodology

3.1 Notations

The dataset consists of n observations, each containing input and outcome images. For $i = 1, \dots, n$, let \mathbf{Z}_i denotes an undirected brain network, represented by a symmetric $V \times V$ matrix. Each entry $z_{i,(v,v')}$ quantifies the connectivity strength between functional nodes \mathcal{G}_v and $\mathcal{G}_{v'}$. These networks are undirected and contain no self-loops, so $z_{i,(v,v')} = z_{i,(v',v)}$, and $z_{i,(v,v)} = 0$. The V functional nodes are together denoted by $\mathcal{G} = \{\mathcal{G}_1, \dots, \mathcal{G}_V\}$. The v th node \mathcal{G}_v contains J_v ROIs, such that the total number of ROIs is $\sum_{v=1}^V J_v = J$. Let $y_i(\mathbf{s}_{v,j}) \in \mathbb{R}$ denote the spatial outcome, and $\mathbf{x}_i(\mathbf{s}_{v,j}) \in \mathbb{R}^Q$ represent spatial inputs at the j th ROI of the v th functional node, with spatial co-ordinate $\mathbf{s}_{v,j} \in \mathbb{R}^d$, for the i th subject. The notation $\mathbf{a} \odot \mathbf{b}$ stands for the Hadamard product describing the elementwise product between two vectors \mathbf{a} and \mathbf{b} . In our context, $y_i(\mathbf{s}_{v,j})$ is the log-transformed BOLDVAR, $\mathbf{x}_i(\mathbf{s}_{v,j})$ represents the vector of GWMIC and CT, while \mathbf{Z}_i is the coactivation network matrix.

3.2 Proposed Explainable Artificial Intelligence (XAI) Model

We propose a two-stage framework: first, we estimate subject-specific overall network connectivity and nodal effects for the V functional nodes from brain networks of subjects, capturing inter-nodal associations in a latent space. Second, we develop an explainable AI framework to predict the outcome image from spatial input images and estimated nodal effects.

3.2.1 First Stage: Estimate Nodal Effects of the Network Predictor

The first stage of our framework fits a parsimonious probabilistic model to the edges of the undirected network predictor \mathbf{Z}_i , for subjects $i = 1, \dots, n$. We represent node interactions within a lower-dimensional latent space that captures the network structure without

imposing overly restrictive assumptions. Specifically, we model the edge weights as:

$$g^{-1}(E[z_{i,(v,v')}|\eta_i, \mathbf{u}_{i,v}, \mathbf{u}_{i,v'}, \sigma_i^2]) = \eta_i - \|\mathbf{u}_{i,v} - \mathbf{u}_{i,v'}\| + \epsilon_{i,(v,v')}, \quad \epsilon_{i,(v,v')} \sim N(0, \sigma_i^2), \quad (1)$$

where $g(\cdot)$ is a link function tailored to the type of edge weights (binary, categorical, or continuous). The parameter η_i captures overall degree of subject-specific network connectivity, while σ_i^2 denotes edge-level variability for the i th subject. The vector $\mathbf{u}_{i,v} = (u_{i,v,1}, \dots, u_{i,v,R})^T \in \mathbb{R}^R$ is a latent coordinate for functional node \mathcal{G}_v for the i th subject, encoding its position in an R -dimensional latent space. The strength of interaction between nodes \mathcal{G}_v and $\mathcal{G}_{v'}$ for subject i is modeled via the Euclidean distance between their latent positions $\mathbf{u}_{i,v}$ and $\mathbf{u}_{i,v'}$ —smaller distances indicate stronger interaction. The parameter R is the intrinsic latent dimension, and may be selected through cross-validation or more adaptive strategies [Guha and Rodriguez, 2021] at a greater computational cost. As model performance is generally stable across a range of R , we opt for fixed R to maintain efficiency.

We assign a prior on each $\eta_i \sim N(0, 1)$ and the priors $\mathbf{u}_{i,v} \stackrel{i.i.d.}{\sim} N(\mathbf{0}, \mathbf{I}_R)$, $\sigma_i^2 \sim IG(\alpha, \beta)$, estimating the joint posterior distribution using Markov Chain Monte Carlo (MCMC) implemented in the `Nimble` software [de Valpine et al., 2017]. Since the model (1) depends on the latent effects $\mathbf{u}_{i,v}$'s only through pairwise distances, it is invariant to the rotation of latent effects. We align estimates across MCMC samples to a common orientation by applying a ‘‘Procrustean transformation’’ [Borg and Groenen, 2005]. Upon the transformation, the latent effects are *comparable* across subjects and across nodes within a subject. Posterior means of the aligned latent nodal estimate $\hat{\mathbf{u}}_{i,v}$ and posterior means for the overall degree of network connectivity $\hat{\eta}_i$ are used as subject-level inputs in the second-stage regression model.

3.2.2 Second Stage: Additive Non-linear Regression Function Estimation Through Deep Neural Networks

In the second stage of our approach, we formulate a non-linear regression function to delineate association between the spatial outcome $y_i(\mathbf{s}_{v,j})$ and spatial inputs $\mathbf{x}_i(\mathbf{s}_{v,j})$, the

estimated overall connectivity $\hat{\eta}_i$ and the estimated nodal effects $\hat{\mathbf{u}}_{i,v}$ corresponding to the v th functional node. Let the features from the network input be denoted by $\mathbf{g}_{i,v} = (\hat{\mathbf{u}}_{i,v}, \hat{\eta}_i)^T$. More precisely, our modeling approach involves

$$y_i(\mathbf{s}_{v,j}) = \mathbf{x}_i(\mathbf{s}_{v,j})^T \boldsymbol{\beta}(\mathbf{s}_{v,j}) + h(\mathbf{g}_{i,v}) + \epsilon_i(\mathbf{s}_{v,j}), \quad j = 1, \dots, J_v; \quad v = 1, \dots, V, \quad (2)$$

where the idiosyncratic errors are assumed to follow $\epsilon_i(\mathbf{s}_{v,j}) \stackrel{i.i.d.}{\sim} N(0, \tau^2)$. Note that the data are mean-standardized. Here $h(\cdot)$ encodes the non-linear relationship between the outcome image at the j th ROI with spatial location $\mathbf{s}_{v,j}$ within the v th functional node, and $\hat{\mathbf{u}}_{i,v}$ and $\hat{\eta}_i$. Although $\hat{\mathbf{u}}_{i,v}$ and $\hat{\eta}_i$ are the latent features used as surrogates for the network predictor, the downstream analysis produces stable predictions with these surrogates. The regression effects of spatial predictors $\mathbf{x}_i(\mathbf{s}_{v,j})$ is encoded in the coefficient vector $\boldsymbol{\beta}(\mathbf{s}_{v,j}) = (\beta_1(\mathbf{s}_{v,j}), \dots, \beta_Q(\mathbf{s}_{v,j}))^T \in \mathbb{R}^Q$ which also varies over spatial locations, and are referred to as varying-coefficients (VCs). VCs combine the flexibility of non-parametric models to capture sufficiently complex dependencies between the outcome and predictors with the interpretability of parametric models [Gelfand et al., 2003, Guhaniyogi et al., 2022].

Traditionally, $\boldsymbol{\beta}(\cdot)$ and $h(\cdot)$ are modeled with Gaussian process (GP) priors, but their estimation is computationally intensive, scaling as $O(J^3)$ and $O(n^3)$. Basis function approximations improve efficiency [Morris, 2015, Reiss et al., 2017] but often oversmooth. Recent scalable GP methods [Guhaniyogi et al., 2022] enhance estimation for large data but still fall short in delivering fast, uncertainty-aware inference needed for modern imaging studies with thousands of subjects and regions.

There is a growing literature on standard deep neural networks (DNNs) to train dependency structures within spatial data [Wikle and Zammit-Mangion, 2023], which is ideal for reducing computational complexity along with capturing spatial dependence. Expanding upon that literature, for $q = 1, \dots, Q$, we model (2) using DNN with dropout vectors applied

to weight matrices and bias vectors, given by,

$$\begin{aligned}\beta_q(\mathbf{s}_{v,j}) &= \sigma_{q,L_\beta}^{(\beta)} \left(\mathbf{W}_{q,L_\beta}^{(\beta)} \sigma_{q,L_\beta-1}^{(\beta)} \left(\cdots \sigma_{q,1}^{(\beta)} \left(\mathbf{W}_{q,1}^{(\beta)} \mathbf{s}_{v,j} + \mathbf{b}_{q,1}^{(\beta)} \right) \odot \mathbf{z}_{q,1}^{(\beta)} \cdots \right) \odot \mathbf{z}_{q,L_\beta-1}^{(\beta)} + \mathbf{b}_{q,L_\beta}^{(\beta)} \right) \\ h(\mathbf{g}_{i,v}) &= \sigma_{L_h}^{(h)} \left(\mathbf{W}_{L_h}^{(h)} \sigma_{L_h-1}^{(h)} \left(\cdots \sigma_1^{(h)} \left(\mathbf{W}_1^{(h)} \mathbf{g}_{i,v} + \mathbf{b}_1^{(h)} \right) \odot \mathbf{z}_1^{(h)} \cdots \right) \odot \mathbf{z}_{L_h-1}^{(h)} + \mathbf{b}_{L_h}^{(h)} \right),\end{aligned}\quad (3)$$

where \odot denotes the element-wise product between two vectors/matrices of the same dimensions, $\sigma_{q,l_1}^{(\beta)}(\cdot)$ is an activation function of the l_1 th layer for the DNN construction of the coefficient function $\beta_q(\cdot)$, $l_1 = 1, \dots, L_\beta$, and $\sigma_{l_2}^{(h)}(\cdot)$ is an activation function of the l_2 th layer for the DNN representation of the function $h(\cdot)$, $l_2 = 1, \dots, L_h$. Assume that the l_1 th layer of the DNN construction of $\beta_q(\cdot)$ and l_2 th layer of DNN construction of $h(\cdot)$ include $k_{l_1}^{(\beta)}$ and $k_{l_2}^{(h)}$ neurons, respectively. The matrix $\mathbf{W}_{q,l_1}^{(\beta)} \in \mathbb{R}^{k_{l_1}^{(\beta)} \times k_{l_1-1}^{(\beta)}}$ is the weight parameters connecting the l_1 and $(l_1 - 1)$ th layer for the DNN construction of $\beta_q(\cdot)$, and $\mathbf{W}_{l_2}^{(h)} \in \mathbb{R}^{k_{l_2}^{(h)} \times k_{l_2-1}^{(h)}}$ is the corresponding matrix connecting the l_2 and $(l_2 - 1)$ th layer for the DNN construction $h(\cdot)$, respectively. The $k_{l_1}^{(\beta)}$ and $k_{l_2}^{(h)}$ dimensional vectors $\mathbf{b}_{q,l_1}^{(\beta)}$ and $\mathbf{b}_{l_2}^{(h)}$ are the bias parameters in the construction of DNN architectures for $\beta_q(\cdot)$ and $h(\cdot)$, respectively. The vectors $\mathbf{z}_{q,l_1}^{(\beta)} \in \mathbb{R}^{k_{l_1-1}^{(\beta)}}$ and $\mathbf{z}_{l_2}^{(h)} \in \mathbb{R}^{k_{l_2-1}^{(h)}}$ have binary entries in $\{0, 1\}$, referred to as the *dropout vectors*, which randomly drop nodes in different layers of a neural network.

A traditional DNN approach proceeds by training the model by minimizing the following loss function with regularization terms as

$$\begin{aligned}\mathcal{L}_{\text{DNN}}(\boldsymbol{\theta}, \tau^2) &= \frac{1}{2N} \sum_{i=1}^n \sum_{v=1}^V \sum_{j=1}^{J_v} \frac{(y_i(\mathbf{s}_{v,j}) - \hat{y}_i(\mathbf{s}_{v,j}))^2}{\tau^2} + \sum_{q=1}^Q \sum_{l_1=1}^{L_\beta} \lambda_{l_1}^{(W, \beta_q)} \left\| \mathbf{W}_{q,l_1}^{(\beta)} \right\|_2^2 \\ &\quad + \sum_{q=1}^Q \sum_{l_1=1}^{L_\beta} \lambda_{l_1}^{(b, \beta_q)} \left\| \mathbf{b}_{q,l_1}^{(\beta)} \right\|_2^2 + \sum_{l_2=1}^{L_h} \lambda_{l_2}^{(W, h)} \left\| \mathbf{W}_{l_2}^{(h)} \right\|_2^2 + \sum_{l_2=1}^{L_h} \lambda_{l_2}^{(b, h)} \left\| \mathbf{b}_{l_2}^{(h)} \right\|_2^2,\end{aligned}\quad (4)$$

where $N = n \times J$, $J = \sum_{v=1}^V J_v$, and $\hat{y}_i(\mathbf{s}_{v,j}) = \mathbf{x}_i(\mathbf{s}_{v,j})^T \boldsymbol{\beta}(\mathbf{s}_{v,j}) + h(\mathbf{g}_{i,v})$ is the point prediction from the model. Here $\boldsymbol{\theta} = \{(\mathbf{W}_{q,l_1}^{(\beta)}, \mathbf{b}_{q,l_1}^{(\beta)}) : q = 1, \dots, Q; l_1 = 1, \dots, L_\beta\} \cup \{(\mathbf{W}_{l_2}^{(h)}, \mathbf{b}_{l_2}^{(h)}) : l_2 = 1, \dots, L_h\}$ denotes the weights and bias parameters for the DNN architecture of $\beta_q(\cdot)$

and $h(\cdot)$. The parameters $\{(\lambda_{l_1}^{(W,\beta_q)}, \lambda_{l_1}^{(b,\beta_q)}) : l_1 = 1, \dots, L_\beta; q = 1, \dots, Q\}$ and $\{(\lambda_{l_2}^{(W,h)}, \lambda_{l_2}^{(b,h)}) : l_2 = 1, \dots, L_h\}$ are penalty parameters controlling shrinkage for weight and bias parameters. Equation (4) imposes regularization on the connections between layers, minimizing the contribution of interconnections between many pairs of neurons in two consecutive layers, preventing DNN from overfitting. The aforementioned DNN framework offers a data-driven optimal point estimate $\hat{\boldsymbol{\theta}}$ for the parameters $\boldsymbol{\theta}$. However, inference requires quantifying uncertainty, naturally achieved through a Bayesian framework by sampling from the posterior distribution of $\boldsymbol{\theta}$ under an appropriate prior. The next section establishes a key connection between deep GPs and dropout-based DNNs, demonstrating that the optimization in (4) corresponds to optimizing variational posterior distribution for a prior on $\boldsymbol{\theta}$. This crucial insight establishes the theoretical backbone of efficient posterior sampling of $\boldsymbol{\theta}$ by applying random dropout to the estimated $\hat{\boldsymbol{\theta}}$ from (4), known as the *MC-dropout* architecture [Gal and Ghahramani, 2016a].

3.2.3 Monte Carlo (MC) Dropout Architecture: Inference from a Deep Neural Network using Deep Gaussian Process

This section establishes that the objective (4) is equivalent to finding optimal parameters of a variational approximation for the posterior distribution of $\boldsymbol{\theta}$ under a deep GP prior construction provided below. This equivalence holds without simplifying assumptions, and leads to a strategy of drawing posterior samples of $\boldsymbol{\theta}$.

Consider a sequence of features $\{\boldsymbol{\psi}_{(v,j)}^{(\beta,q,l_1)} \in \mathbb{R}^{k_{l_1}^{(\beta)}} : j = 1, \dots, J_v; v = 1, \dots, V; l_1 = 1, \dots, L_\beta\}$ over L_β layers, with the features in the l_1 th layer is of dimension $k_{l_1}^{(\beta)}$. Let $\boldsymbol{\Psi}_{q,l_1}^{(\beta)} = \left[\boldsymbol{\psi}_{(1,1)}^{(\beta,q,l_1)} : \dots : \boldsymbol{\psi}_{(1,J_1)}^{(\beta,q,l_1)} : \dots : \boldsymbol{\psi}_{(V,1)}^{(\beta,q,l_1)} : \dots : \boldsymbol{\psi}_{(V,J_V)}^{(\beta,q,l_1)} \right]^T$ denote a $J \times k_{l_1}^{(\beta)}$ matrix obtained by stacking features in the l_1 th layer. Let the k th column of this matrix is denoted as $\boldsymbol{\psi}_{q,l_1,k}^{(\beta)}$. Assuming conditional independence of $\boldsymbol{\psi}_{q,l_1,k}^{(\beta)}$ over k , we model $\beta_q(\cdot)$ using a deep GP with L_β layers. Conditional on the features in the $(l_1 - 1)$ th layer, the realizations at the l_1 th layer follow

$$\boldsymbol{\psi}_{q,l_1,k}^{(\beta)} | \boldsymbol{\Psi}_{q,l_1-1}^{(\beta)} \sim N(\mathbf{0}, \boldsymbol{\Sigma}_{q,l_1}^{(\beta)}), \quad k = 1, \dots, k_{l_1}^{(\beta)}, \quad l_1 = 1, \dots, L_\beta, \quad (5)$$

with the coefficients $\beta_q(\mathbf{s}_{v,j})$ being constructed through the L_β th layer of the features. Specifically, if $\boldsymbol{\beta}_q$ is a J dimensional vector $(\beta_q(\mathbf{s}_{v,j}) : j = 1, \dots, J; v = 1, \dots, V)^T$, then we model $\boldsymbol{\beta}_q = \sigma_{q,L_\beta}^{(\beta)}(\boldsymbol{\Psi}_{q,L_\beta}^{(\beta)})$. The covariance matrix $\boldsymbol{\Sigma}_{q,l_1}^{(\beta)} \in \mathbb{R}^{J \times J}$ depends on features from the previous layer. Let $\boldsymbol{\Phi}_{q,l_1}^{(\beta)} = [\boldsymbol{\phi}_{(1,1)}^{(\beta,q,l_1)} : \dots : \boldsymbol{\phi}_{(1,J_1)}^{(\beta,q,l_1)} : \dots : \boldsymbol{\phi}_{(V,1)}^{(\beta,q,l_1)} : \dots : \boldsymbol{\phi}_{(V,J_V)}^{(\beta,q,l_1)}]^T$ be a $J \times k_{l_1}^{(\beta)}$ dimensional matrix of feature vectors after applying transformation through the activation function, such that $\boldsymbol{\phi}_{(v,j)}^{(\beta,q,l_1)} = \sigma_{q,l_1}^{(\beta)}(\boldsymbol{\psi}_{(v,j)}^{(\beta,q,l_1)})$. The covariance matrix $\boldsymbol{\Sigma}_{q,l_1}^{(\beta)}$ is expressed as

$$\boldsymbol{\Sigma}_{q,l_1}^{(\beta)} = \frac{1}{k_{l_1}^{(\beta)}} \sigma_{q,l_1}^{(\beta)} (\boldsymbol{\Phi}_{q,l_1-1}^{(\beta)} \mathbf{W}_{q,l_1}^{(\beta)\top} + \mathbf{b}_{q,l_1}^{(\beta)}) \sigma_{q,l_1}^{(\beta)} (\boldsymbol{\Phi}_{q,l_1-1}^{(\beta)} \mathbf{W}_{q,l_1}^{(\beta)\top} + \mathbf{b}_{q,l_1}^{(\beta)})^\top. \quad (6)$$

Similarly, define a sequence of features $\{\boldsymbol{\psi}_{(i,v)}^{(h,l_2)} \in \mathbb{R}^{k_{l_2}^{(h)}} : i = 1, \dots, n; v = 1, \dots, V; l_2 = 1, \dots, L_h\}$ and construct non-linear transformation $\{\boldsymbol{\phi}_{(i,v)}^{(h,l_2)} : i = 1, \dots, n; v = 1, \dots, V; l_2 = 1, \dots, L_h\}$ of these features after applying the activation function, such that $\boldsymbol{\phi}_{(i,v)}^{(h,l_2)} = \sigma_{l_2}^{(h)}(\boldsymbol{\psi}_{(i,v)}^{(h,l_2)}) \in \mathbb{R}^{k_{l_2}^{(h)}}$. Collapsing the three-way tensor $\{\boldsymbol{\psi}_{(i,v)}^{(h,l_2)}\}_{i=1,v=1}^{n,V} \in \mathbb{R}^{n \times V \times k_{l_2}^{(h)}}$ along the third mode leads to a $(nV) \times k_{l_2}^{(h)}$ matrix $\boldsymbol{\Psi}_{l_2}^{(h)}$, whose k th column is denoted as $\boldsymbol{\psi}_{l_2,k}^{(h)}$. Assuming independence of $\boldsymbol{\psi}_{l_2,k}^{(h)}$ across k , we model $h(\cdot)$ using a deep GP with L_h layers. Specifically, conditional on the parameters in $(l_2 - 1)$ th layer, the finite-dimensional realizations of the l_2 th layer follow

$$\boldsymbol{\psi}_{l_2,k}^{(h)} | \boldsymbol{\Psi}_{l_2-1}^{(h)} \sim N(0, \boldsymbol{\Sigma}_{l_2}^{(h)}), \quad k = 1, \dots, k_{l_2}^{(h)}, \quad l_2 = 1, \dots, L_h, \quad (7)$$

with the non-linear function $h(\mathbf{g}_{i,v})$ being constructed through the L_h th layer of the features, i.e., if \mathbf{h} is an nV dimensional vector obtained by vectorizing the $n \times V$ dimensional matrix $(h(\mathbf{g}_{i,v}))_{i,v=1}^{n,V}$, then we model $\mathbf{h} = \sigma_{L_h}^{(h)}(\boldsymbol{\Psi}_{L_h}^{(h)})$. Let $\boldsymbol{\Phi}_{l_2}^{(h)}$ is a $(nV) \times k_{l_2}^{(h)}$ matrix formed by collapsing the $n \times V \times k_{l_2}^{(h)}$ tensor $\{\boldsymbol{\phi}_{(i,v)}^{(h,l_2)}\}_{i,v=1}^{n,V}$ in the third mode. We covariance matrix $\boldsymbol{\Sigma}_{l_2}^{(h)}$ is constructed as

$$\boldsymbol{\Sigma}_{l_2}^{(h)} = \frac{1}{k_{l_2}^{(h)}} \sigma_{l_2}^{(h)} (\boldsymbol{\Phi}_{l_2-1}^{(h)} \mathbf{W}_{l_2}^{(h)\top} + \mathbf{b}_{l_2}^{(h)}) \sigma_{l_2}^{(h)} (\boldsymbol{\Phi}_{l_2-1}^{(h)} \mathbf{W}_{l_2}^{(h)\top} + \mathbf{b}_{l_2}^{(h)})^\top. \quad (8)$$

Assuming that the final layer in both generative models consists of one component, i.e.,

$k_{L_\beta}^{(\beta)} = k_{L_h}^{(h)} = 1$, the proposed generative model is given by,

$$y_i(\mathbf{s}_{v,j}) | \{\Psi_{q,L_\beta}^{(\beta)}\}_{q=1}^Q, \Psi_{L_h}^{(h)}, \tau^2, \mathbf{x}(\mathbf{s}_i), \mathbf{g}_{i,v} \sim N(\mathbf{x}_i(\mathbf{s}_{v,j})^T \boldsymbol{\beta}(\mathbf{s}_{v,j}) + h(\mathbf{g}_{i,v}), \tau^2),$$

$$\beta_q(\mathbf{s}_{v,j}) = \sigma_{q,L_\beta}^{(\beta)}(\psi_{(v,j)}^{(\beta,q,L_\beta)}), h(\mathbf{g}_{i,v}) = \sigma_{L_h}^{(h)}(\psi_{(i,v)}^{(h,L_h)}), i = 1, \dots, n; q = 1, \dots, Q; j = 1, \dots, J_v; v = 1, \dots, V$$

$$\psi_{q,l_1,k}^{(\beta)} | \Psi_{q,l_1-1}^{(\beta)} \sim N(\mathbf{0}, \Sigma_{q,l_1}^{(\beta)}), q = 1, \dots, Q; k = 1, \dots, k_{l_1}^{(\beta)}; l_1 = 1, \dots, L_\beta$$

$$\psi_{l_2,k}^{(h)} | \Psi_{l_2-1}^{(h)} \sim N(\mathbf{0}, \Sigma_{l_2}^{(h)}), k = 1, \dots, k_{l_2}^{(h)}, l_2 = 1, \dots, L_h. \quad (9)$$

Figure 2 illustrates the proposed explainable AI (XAI) approach.

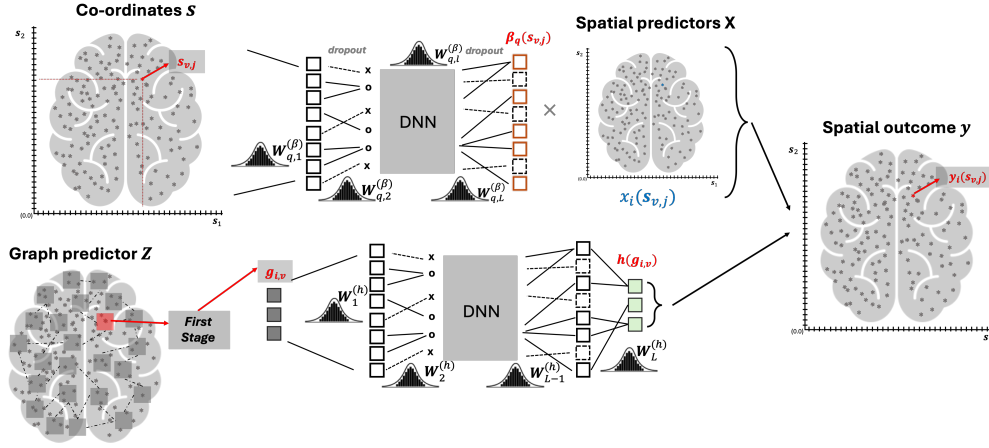


Figure 2: Illustration for the XAI.

We adopt variational Bayesian inference called *MC dropout*, to approximate posterior distribution of $\boldsymbol{\theta}$. Let $\mathbf{D} = \{\{\{\mathbf{x}_i(\mathbf{s}_{v,j}), \mathbf{s}_{v,j}, \mathbf{g}_{i,v}\}_{j=1}^{J_v}\}_{v=1}^V\}_{i=1}^n$ denote the input data. For Bayesian inference, independent standard normal priors are set on each component of the weight and bias parameters, denoted by $p(\boldsymbol{\theta}) = N(\mathbf{0}, \mathbf{I})$. We construct a variational approximation of the posterior distribution of parameters $\tilde{q}(\boldsymbol{\theta})$, constructed as $\tilde{q}(\boldsymbol{\theta}) := \prod_{l_1=1}^{L_\beta} \prod_{q=1}^Q \tilde{q}(\mathbf{W}_{q,l_1}^{(\beta)}, \mathbf{b}_{q,l_1}^{(\beta)}) \prod_{l_2=1}^{L_h} \tilde{q}(\mathbf{W}_{l_2}^{(h)}, \mathbf{b}_{l_2}^{(h)})$ where each term represents the variational distribution of the corresponding weight matrices and bias vectors. Let $\mathbf{w}_{q,l_1,t}^{(\beta)} = (w_{l_1,j,tp}^{(\beta)} : p = 1, \dots, k_{l_1-1}^{(\beta)})$ and $\mathbf{w}_{l_2,t}^{(h)} = (w_{l_2,tp}^{(h)} : p = 1, \dots, k_{l_2-1}^{(h)})$ be the t th row of the matrices $\mathbf{W}_{q,l_1}^{(\beta)}$ and $\mathbf{W}_{l_2}^{(h)}$, respectively. The variational distribution is

constructed as

$$\begin{aligned}
\tilde{q}(\mathbf{W}_{q,l_1}^{(\beta)}, \mathbf{b}_{q,l_1}^{(\beta)}) &= \prod_{\forall t} \tilde{q}(\mathbf{w}_{q,l_1,t}^{(\beta)}, b_{q,l_1,t}^{(\beta)}), \quad \tilde{q}(\mathbf{W}_{l_2}^{(h)}, \mathbf{b}_{l_2}^{(h)}) = \prod_{\forall t} \tilde{q}(\mathbf{w}_{l_2,t}^{(h)}, b_{l_2,t}^{(h)}) \\
\tilde{q}(\mathbf{w}_{q,l_1,t}^{(\beta)}, b_{q,l_1,t}^{(\beta)}) &= p_{l_1}^{(\beta)} N((\boldsymbol{\mu}_{q,l_1,t}^{w,(\beta)}, \mu_{q,l_1,t}^{b,(\beta)})^\top, \sigma^2 \mathbf{I}) + (1 - p_{l_1}^{(\beta)}) N(\mathbf{0}, \sigma^2 \mathbf{I}), \\
\tilde{q}(\mathbf{w}_{l_2,t}^{(h)}, b_{l_2,t}^{(h)}) &= p_{l_2}^{(h)} N((\boldsymbol{\mu}_{l_2,t}^{w,(h)}, \mu_{l_2,t}^{b,(h)})^\top, \sigma^2 \mathbf{I}) + (1 - p_{l_2}^{(h)}) N(\mathbf{0}, \sigma^2 \mathbf{I}), \tag{10}
\end{aligned}$$

where $l_1 = 1, \dots, L_\beta$ and $l_2 = 1, \dots, L_h$. The parameters $w_{q,l_1,tp}^{(\beta)}$ and $w_{l_2,tp}^{(h)}$ are the (t,p) th element of the weight matrices $\mathbf{W}_{q,l_1}^{(\beta)}$ and $\mathbf{W}_{l_2}^{(h)}$, respectively. Similarly, $b_{q,l_1,t}^{(\beta)}$ and $b_{l_2,t}^{(h)}$ are the t th element of the bias vectors $\mathbf{b}_{q,l_1}^{(\beta)}$ and $\mathbf{b}_{l_2}^{(h)}$, respectively. Each scalar weight or bias has a variational distribution of the Gaussian mixture, with each mixing component having a small variance σ^2 . Let $\boldsymbol{\Delta}$ denote the collection of variational parameters $\{\boldsymbol{\mu}_{q,l_1,t}^{w,(\beta)} = (\mu_{q,l_1,tp}^{w,(\beta)} : p = 1, \dots, k_{l_1-1}^{(\beta)}) : l_1 = 1, \dots, L_\beta; t = 1, \dots, k_{l_1}^{(\beta)}; q = 1, \dots, Q\}$, $\{\boldsymbol{\mu}_{l_2,t}^{w,(h)} = (\mu_{l_2,tp}^{w,(h)} : p = 1, \dots, k_{l_2-1}^{(h)}) : l_2 = 1, \dots, L_h; t = 1, \dots, k_{l_2}^{(h)}\}$, $\{\boldsymbol{\mu}_{q,l_1,t}^{b,(\beta)} : l_1 = 1, \dots, L_\beta; t = 1, \dots, k_{l_1}^{(\beta)}; q = 1, \dots, Q\}$, $\{\boldsymbol{\mu}_{l_2,t}^{b,(h)} : l_2 = 1, \dots, L_h; t = 1, \dots, k_{l_2}^{(h)}\}$ and σ^2 . Under the mixture normal specification for the variational distribution of all weight and bias parameters, as the inclusion probabilities $p_{l_1}^{(\beta)}, p_{l_2}^{(h)} \in [0, 1]$ approaches 0, $\tilde{q}(\mathbf{w}_{q,l_1,t}^{(\beta)})$ and $\tilde{q}(\mathbf{w}_{l_2,t}^{(h)})$ becomes close to $N(\mathbf{0}, \sigma^2 \mathbf{I})$. We denote the variational distribution as $\tilde{q}(\boldsymbol{\theta}|\boldsymbol{\Delta})$ to explicitly show its dependence on the variational parameters. The optimal variational parameters are set by maximizing

$$\mathbb{E}_{\tilde{q}}[\log(\pi(\boldsymbol{\theta}, \mathbf{D}))] - \mathbb{E}_{\tilde{q}}[\log \tilde{q}(\boldsymbol{\theta}|\boldsymbol{\Delta})], \tag{11}$$

the evidence lower bound (ELBO), where $\pi(\boldsymbol{\theta}, \mathbf{D})$ is the joint distribution of data \mathbf{D} and parameters $\boldsymbol{\theta}$. Let $\boldsymbol{\theta}^{(m)} = \{\{\mathbf{W}_{q,l_1}^{(\beta)(m)}, \mathbf{b}_{q,l_1}^{(\beta)(m)}\}_{l_1=1,q=1}^{L_\beta,Q}, \{\mathbf{W}_{l_2}^{(h)(m)}, \mathbf{b}_{l_2}^{(h)(m)}\}_{l_2=1}^{L_h}\}$ be MC samples from the variational distribution in (10). The detailed derivations in Section 1 of the

supplementary file show that an MC approximation of ELBO is given by,

$$\begin{aligned} \mathcal{L}_{\text{GP-MC}}(\tau^2, \Delta) &\approx \frac{1}{M} \sum_{m=1}^M \sum_{i=1}^n \sum_{v=1}^V \sum_{j=1}^{J_v} \log p(\mathbf{y}_i(\mathbf{s}_{v,j}) | \mathbf{x}_i(\mathbf{s}_{v,j}), \mathbf{g}_{i,v}, \tau^2, \boldsymbol{\theta}^{(m)}) - \\ &\sum_{l_1=1}^{L_\beta} \sum_{q=1}^Q \frac{p_{l_1}^{(\beta)}}{2} (\|\boldsymbol{\mu}_{q,l_1}^{w,(\beta)}\|_2^2) - \sum_{l_1=1}^{L_\beta} \sum_{q=1}^Q \frac{p_{l_1}^{(\beta)}}{2} (\|\boldsymbol{\mu}_{q,l_1}^{b,(\beta)}\|_2^2) - \sum_{l_2=1}^{L_h} \frac{p_{l_2}^{(h)}}{2} (\|\boldsymbol{\mu}_{l_2}^{w,(h)}\|_2^2) - \sum_{l_2=1}^{L_h} \frac{p_{l_2}^{(h)}}{2} (\|\boldsymbol{\mu}_{l_2}^{b,(h)}\|_2^2). \end{aligned} \quad (12)$$

The data likelihood $p(\mathbf{y}_i(\mathbf{s}_{v,j}) | \mathbf{x}_i(\mathbf{s}_{v,j}), \mathbf{g}_{i,v}, \tau^2, \boldsymbol{\theta}^{(m)})$ is given by the normal distribution in the first row of (9).

Approximating posterior samples of DNNs using MC dropout. By setting $\lambda_{l_1}^{(W, \beta_q)}$, $\lambda_{l_1}^{(b, \beta_q)}$, $\lambda_{l_2}^{(W, h)}$, and $\lambda_{l_2}^{(b, h)}$ as $\frac{p_{l_1}^{(\beta)}}{2N}$, $\frac{p_{l_1}^{(\beta)}}{2N}$, $\frac{p_{l_2}^{(h)}}{2N}$ and $\frac{p_{l_2}^{(h)}}{2N}$, respectively, the negative of the objective function (12) after scaling with $1/N$ becomes equivalent to (4). Details of the derivation are provided in Section 1 of the supplementary file. This reveals that finding optimal $\hat{\boldsymbol{\theta}}$ from a DNN with dropout by minimizing the objective function (4), is mathematically equivalent to estimating the optimal variational parameters $\hat{\Delta}$ by maximizing the objective function (12). This is a highly consequential result, as it allows efficient estimation of variational parameters $\hat{\Delta}$ by optimizing the loss function in (4) using an efficient stochastic gradient descent (SGD) algorithm. Assuming $\sigma^2 \approx 0$, approximate posterior samples of the weights and biases $\boldsymbol{\theta}$ can then be drawn by applying dropout to $\hat{\boldsymbol{\theta}}$. To elaborate on it, for each layer l_1 , generate vectors of Bernoulli random variables $\mathbf{z}_{q,l_1}^{(\beta)} \in \{0, 1\}^{k_{l_1}^{(\beta)}}$ with keep probability $1 - p_{l_1}^{(\beta)}$. Then construct a dropout mask of binary elements $\mathbf{Z}_{q,l_1}^{(\beta)} = \mathbf{z}_{q,l_1}^{(\beta)} \mathbf{1}_{k_{l_1}^{(\beta)}}^\top \in \mathbb{R}^{k_{l_1}^{(\beta)} \times k_{l_1}^{(\beta)-1}}$ for the l_1 th layer for weights corresponding to DNN architecture of $\beta_q(\cdot)$. Similarly, each layer l_2 , generate vectors of Bernoulli random variables $\mathbf{z}_{q,l_2}^{(h)} \in \{0, 1\}^{k_{l_2}^{(h)}}$, and construct each element of the dropout mask $\mathbf{Z}_{l_2}^{(h)} = \mathbf{z}_{q,l_2}^{(h)} \mathbf{1}_{k_{l_2}^{(h)}}^\top \in \mathbb{R}^{k_{l_2}^{(h)} \times k_{l_2}^{(h)-1}}$ for l_2 th layer for weights for the DNN construction of $h(\cdot)$. We apply dropout masks $\mathbf{Z}_{q,l_1}^{(\beta)}$, $\mathbf{z}_{q,l_1}^{(\beta)}$, $\mathbf{Z}_{l_2}^{(h)}$ and $\mathbf{z}_{l_2}^{(h)}$ to the estimated weight matrices and bias vectors $\widehat{\mathbf{W}}_{q,l_1}^{(\beta)}$, $\widehat{\mathbf{b}}_{q,l_1}^{(\beta)}$, $\widehat{\mathbf{W}}_{l_2}^{(h)}$ and $\widehat{\mathbf{b}}_{l_2}^{(h)}$ (obtained by optimizing (4)), respectively, to obtain $\widehat{\mathbf{W}}_{q,l_1}^{(\beta)} \odot \mathbf{Z}_{q,l_1}^{(\beta)}$, $\widehat{\mathbf{b}}_{q,l_1}^{(\beta)} \odot \mathbf{z}_{q,l_1}^{(\beta)}$, $\widehat{\mathbf{W}}_{l_2}^{(h)} \odot \mathbf{Z}_{l_2}^{(h)}$ and $\widehat{\mathbf{b}}_{l_2}^{(h)} \odot \mathbf{z}_{l_2}^{(h)}$. Given $\sigma^2 \approx 0$,

these corresponds to approximate draws from the marginal variational posteriors of $\mathbf{W}_{q,l_1}^{(\beta)}$, $\mathbf{b}_{q,l_1}^{(\beta)}$, $\mathbf{W}_{l_2}^{(h)}$ and $\mathbf{b}_{l_2}^{(h)}$ in (10), respectively.

Repeating this procedure F times yields F approximate posterior samples from the DNNs, which are further used for posterior inference of model parameters and posterior predictive inference. Details of the algorithm are presented in Algorithm 1.

Algorithm 1: Explainable AI Algorithm

- 1 **Step 1:** Initialize parameters $\boldsymbol{\theta}$ at $\boldsymbol{\theta}^{(0)}$;
 - 2 **Step 2:** Find the optimal point estimates $\boldsymbol{\theta}$ using SGD;
 - 3 **for** $iter = 1$ **to** n_{iter} **do**
 - 4 Update $\boldsymbol{\theta}$ using SGD to minimize loss function in Eq. (4);
 - 5 **Return:** Optimized estimates $\hat{\boldsymbol{\theta}} = \left\{ \begin{array}{l} \{\widehat{\mathbf{W}}_{q,l_1}^{(\beta)}, \widehat{\mathbf{b}}_{q,l_1}^{(\beta)}\}_{l_1=1,q=1}^{L_\beta,Q} \\ \{\widehat{\mathbf{W}}_{l_2}^{(h)}, \widehat{\mathbf{b}}_{l_2}^{(h)}\}_{l_2=1}^{L_h} \end{array} \right\}, \hat{\beta}_0$;
 - 6 **Step 3:** Draw samples of $\boldsymbol{\theta}$ and τ^2 using dropout;
 - 7 **for** $f = 1$ **to** F **do**
 - 8 Sample dropout masks;
 - 9 For $l_1 = 1, \dots, L_\beta$, $q = 1, \dots, Q$, sample node-wise dropout mask $\mathbf{z}_{q,l_1}^{(\beta)(f)} \in \mathbb{R}^{k_{l_1}^{(\beta)}}$ from Bernoulli($1 - p_{l_1}^{(\beta)}$) and set $\mathbf{Z}_{q,l_1}^{(\beta)(f)} = \mathbf{z}_{q,l_1}^{(\beta)(f)} \mathbf{1}_{k_{l_1}^{(\beta)}}^\top$.
 - 10 Similarly, for $l_2 = 1, \dots, L_h$, sample node-wise dropout mask $\mathbf{z}_{l_2}^{(h)(f)} \in \mathbb{R}^{k_{l_2}^{(h)}}$ from Bernoulli($1 - p_{l_2}^{(h)}$) and set $\mathbf{Z}_{l_2}^{(h)(f)} = \mathbf{z}_{l_2}^{(h)(f)} \mathbf{1}_{k_{l_2}^{(h)}}^\top$.
 - 11 Apply masks element-wise to $\hat{\boldsymbol{\theta}}$ to obtain sparse $\boldsymbol{\theta}^{(f)}$;
 - 12 i.e., set $\widehat{\mathbf{W}}_{q,l_1}^{(\beta)} \odot \mathbf{Z}_{q,l_1}^{(\beta)(f)}$, $\widehat{\mathbf{b}}_{q,l_1}^{(\beta)} \odot \mathbf{z}_{q,l_1}^{(\beta)(f)}$, $\widehat{\mathbf{W}}_{l_2}^{(h)} \odot \mathbf{Z}_{l_2}^{(h)(f)}$ and $\widehat{\mathbf{b}}_{l_2}^{(h)} \odot \mathbf{z}_{l_2}^{(h)(f)}$.
 - 13 Compute $\beta_q(\mathbf{s}_{v,j})^{(f)}$ and $h(\mathbf{g}_{i,v})^{(f)}$ using Eq. (3) from $\boldsymbol{\theta}^{(f)}$;
 - 14 Compute variance: $\tau^{2(f)} = \frac{1}{n \sum_v J_v} \sum_{i=1}^n \sum_{v=1}^V \sum_{j=1}^{J_v} \left(y_i(\mathbf{s}_{v,j}) - \hat{\beta}_0 - \mathbf{x}_i(\mathbf{s}_{v,j})^T \boldsymbol{\beta}^{(f)}(\mathbf{s}_{v,j}) - h^{(f)}(\mathbf{g}_{i,v}) \right)^2$;
 - 15 **Step 4:** **return** Approximate posterior samples: $\{\boldsymbol{\theta}^{(1)}, \dots, \boldsymbol{\theta}^{(F)}\}, \{\tau^{2(1)}, \dots, \tau^{2(F)}\}$;
-

3.3 Explainable Inference with Deep Neural Network

A key feature of XAI is ability to quantify uncertainty in the estimation of the spatially-varying image predictor coefficients $\beta_q(\cdot)$, the function representing node effects $h(\cdot)$, and in the prediction of the outcome image, thereby enabling *explainable inference* within deep neural networks. Let $\mathbf{D} = \{(y_i(\mathbf{s}_{v,j}), \mathbf{x}_i(\mathbf{s}_{v,j}), \mathbf{g}_{i,v})^T : i = 1, \dots, n; j = 1, \dots, J_v; v = 1, \dots, V\}$

denote the observed data. To predict unobserved outcome $y_{i^*}(\mathbf{s}_{v,j})$ for a new sample indexed i^* , we first employ the algorithm outlined in Section 3.2.1 to construct the features $\{\mathbf{g}_{i^*,v} : v = 1, \dots, V\}$ from the graph predictor \mathbf{Z}_{i^*} for the new sample. The posterior predictive distribution is then given by $p(y_{i^*}(\mathbf{s}_{v,j})|\mathbf{D}) = \int \cdots \int N(y_{i^*}(\mathbf{s}_{v,j})|\mathbf{x}_{i^*}(\mathbf{s}_{v,j})^T \boldsymbol{\beta}(\mathbf{s}_{v,j}) + h(\mathbf{g}_{i^*,v}), \tau^2) \pi(\boldsymbol{\theta}|\mathbf{D}) d\boldsymbol{\theta} d\tau^2$. Since it is challenging to compute the posterior predictive distribution directly, we approximate it through the samples of $\boldsymbol{\theta}, \tau^2$. With approximate posterior samples $\{\boldsymbol{\theta}^{(f)}, \tau^{2(f)}\}_{f=1}^F$ drawn following Algorithm 1, we adopt composition sampling, wherein the f th post burn-in iterate $y_{i^*}^{(f)}(\mathbf{s}_{v,j})$ is drawn from $N(y_{i^*}(\mathbf{s}_{v,j})|\mathbf{x}_{i^*}(\mathbf{s}_{v,j})^T \boldsymbol{\beta}(\mathbf{s}_{v,j})^{(f)} + h(\mathbf{g}_{i^*,v})^{(f)}, \tau^{2(f)})$.

Inference on $h(\mathbf{g}_{i,v})$ is based on approximate posterior samples of $\{h(\mathbf{g}_{i,v})^{(f)}\}_{f=1}^F$ constructed from (3) using samples $\{\boldsymbol{\theta}^{(f)}\}_{f=1}^F$. Although $\beta_q(\mathbf{s}_{v,j})$ can be directly inferred from its approximate posterior samples $\{\beta_q(\mathbf{s}_{v,j})^{(f)} : f = 1, \dots, F\}$, we observe slight under-coverage in the resulting credible intervals. Thus, we approximate its posterior with a normal distribution, using empirical mean $\mu_q(\mathbf{s}_{v,j}) = \frac{1}{F} \sum_{f=1}^F \beta_q(\mathbf{s}_{v,j})^{(f)}$ and variance $\sigma_q^2(\mathbf{s}_{v,j}) = \frac{1}{F-1} \sum_{f=1}^F (\beta_q(\mathbf{s}_{v,j})^{(f)} - \mu_q(\mathbf{s}_{v,j}))^2$, and generate refined samples from $N(\mu_q(\mathbf{s}_{v,j}), \sigma_q^2(\mathbf{s}_{v,j}))$.

4 Simulation Study

This section evaluates the performance of XAI alongside relevant Bayesian linear, non-linear, and deep learning methods for image-on-image regression, focusing on three key aspects: predictive inference, inference on the spatially-varying predictor coefficients $\boldsymbol{\beta}_q(\cdot)$, and inference on $h(\cdot)$, which captures the non-linear effect of the network predictor.

4.1 Simulation Design

In all simulations, the spatial locations $\mathbf{s}_{v,j}$ are assumed to be three-dimensional ($d = 3$) and are drawn uniformly from the domain $[0, 2] \times [0, 2] \times [0, 2]$. Each simulation assumes $Q = 2$, sets $\mathbf{x}_i(\mathbf{s}_{v,j}) = \mathbf{x}_i \in \mathbb{R}^Q$ for all v, j , and draws \mathbf{x}_i from $N(0, \mathbf{I}_2)$. The spatial predictor coefficients in $\beta_q(\cdot)$ ($q = 1, 2$) are simulated from a Gaussian process (GP) with mean zero and an exponential covariance function, characterized by the spatial variance $\delta_{\beta,q}^2$ and the spatial

scale parameter $\eta_{\beta,q}$. Specifically, $\text{Cov}(\beta_q(\mathbf{s}_{v,j}), \beta_q(\mathbf{s}_{v',j'})) = \delta_{\beta,q}^2 \exp(-\|\mathbf{s}_{v,j} - \mathbf{s}_{v',j'}\|_2 / \eta_{\beta,q})$, for any $v, v' = 1, \dots, V$, $j = 1, \dots, J_v$ and $j' = 1, \dots, J_{v'}$. The latent network effects $\mathbf{g}_{i,v}$'s are simulated from $N(0, \mathbf{I}_2)$. The regression function $h(\cdot)$ for the latent network effect is modeled as a Gaussian process with mean zero and an exponential covariance kernel, defined by the spatial variance parameter δ_h^2 and spatial scale parameter η_h . Each simulation uses a sample size of 300 with low signal-to-noise ratio (SNR) to reflect real neuroimaging data. The response is generated using equation (2) with noise variance $\tau^2 = 4$. Of the 300 samples, 180 are used for training, 60 for validation, and $n^* = 60$ for testing. Simulations assume equal regions per node, i.e., $J_1 = \dots = J_V$, and fix the number of network nodes at $V = 30$.

We explore simulation scenarios by varying the total number of regions J . Additionally, different combinations of $(\delta_{\beta,1}^2, \delta_{\beta,2}^2, \eta_{\beta,1}, \eta_{\beta,2}, \delta_h^2, \eta_h)$ induce varying SNR levels, allowing us to assess model performance under a range of SNRs. Simulation results on the effect of varying correlation parameters are presented in Section 2 of the supplementary file.

4.2 Competitors and Metric of Comparison

We implement the proposed XAI approach in TensorFlow with ReLU activation function in all hidden layers and run all experiments on a 4-core, 2.3 GHz Intel Core i7 processor. The objective function in (4) is optimized using the Adam optimizer with an initial learning rate of 10^{-2} , a decay rate of 0.97, and decay steps of 10,000. For the scenario that varies the total number of ROIs, we use a batch size of 10 and a maximum of 300 training epochs, whereas for the scenario that varies the signal-to-noise ratios, the batch size is 20 with a maximum of 500 epochs. We apply early stopping based on the validation mean squared error, using a patience of 8 epochs and a minimum improvement threshold of 10^{-4} , and we restore the weights corresponding to the best validation performance. To evaluate performance, we compare XAI's predictions and estimation of $\beta_q(\cdot)$ and $h(\cdot)$ against Bayesian Additive Regression Trees (BART) [Chipman et al., 2010], BIRD-GP [Ma et al., 2023], and a Generalized Linear Model (GLM). For fair comparison, BART includes spatial coordinates along with imaging and network inputs. While GLM is commonly used in image-on-image regression [Batouli

and Sisakhti, 2020], it lacks non-linear modeling and uncertainty quantification. BART also ignores structural differences by stacking network and spatial objects into a single input. For BIRD-GP, we use 30 basis functions and optimize the model with 2,500 gradient steps, while for BART, we employ an ensemble of 200 trees across all scenarios.

To evaluate predictive performance, we report root mean square prediction error (RM-SPE), empirical coverage, and average length of 95% prediction intervals over n^* test samples. Inference on $\beta_q(\cdot)$ and $h(\cdot)$ is assessed with root mean square error (RMSE), coverage, and length of 95% credible intervals. Inference on $\beta_q(\cdot)$ and $h(\cdot)$ is available only for XAI and GLM, as BART and BIRD-GP do not support it. Each simulation is repeated 100 times.

4.3 Simulation Results

4.3.1 Impact of Changing the Total Number of ROIs (J)

To evaluate the impact of the number of ROIs, we consider four simulation cases by varying the total number of ROIs J between 150 to 1200 across four cases (see Table 1). For all four cases, the variance parameters and scale parameters are kept fixed at $(\delta_{\beta,1}^2, \delta_{\beta,2}^2, \delta_h^2) = (2, 1, 2.5)$ and $(\eta_{\beta,1}, \eta_{\beta,2}, \eta_h) = (5, 4, 6)$.

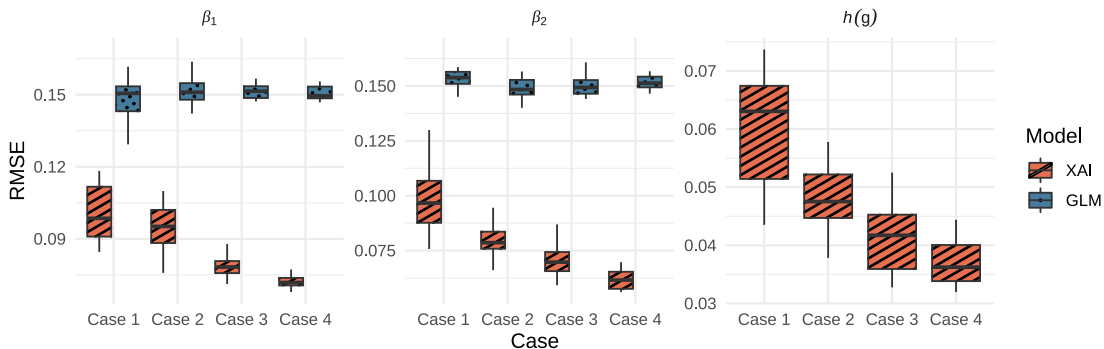


Figure 3: Root mean squared error (RMSE) comparison between the proposed XAI method and GLM for estimating the spatially varying coefficients $\beta_1(\mathbf{s})$ and $\beta_2(\mathbf{s})$, and the network latent effect $h(\mathbf{g})$ under Case 1 to Case 4. Boxplots show the distribution of RMSE across 100 simulation replications. The inference on $\beta_1(\mathbf{s})$, $\beta_2(\mathbf{s})$, $h(\mathbf{g})$ are not available for BART and BIRD-GP. The inference on $h(\mathbf{g})$ is not available for GLM.

Figure 3 shows that XAI consistently yields lower RMSE than GLM across varying val-

ues of J when estimating $\beta_1(\mathbf{s})$, $\beta_2(\mathbf{s})$ and $h(\mathbf{g})$. While GLM assumes a linear relationship between the network latent effect and the outcome, XAI flexibly captures complex nonlinear dependencies through its estimation of the nonlinear function $h(\mathbf{g})$. Furthermore, the GLM framework fits separate regression coefficients for each ROI without leveraging spatial correlations, resulting in stable but less adaptive point estimates with decreasing standard errors as J increases. In contrast, XAI exhibits notable improvements in estimation accuracy with larger J , owing to its ability to borrow information spatially for estimating $\beta_1(\mathbf{s})$ and $\beta_2(\mathbf{s})$, and across the network latent space for $h(\mathbf{g})$.

Table 1: Prediction performance comparison for simulated datasets under Case 1 to Case 4. The table reports the root mean squared prediction error (RMSPE) with standard errors in parentheses for each method (XAI, BART, BIRD-GP, and GLM). The standard errors are presented over 100 replications. Best performing model is boldfaced in each case.

J	Cases	XAI	BART	BIRD-GP	GLM
150	Case 1	2.0101(0.011)	2.0148(0.010)	3.0234(1.0993)	2.0264(0.011)
300	Case 2	2.0020(0.011)	2.0093(0.010)	2.6435(0.4559)	2.0247(0.007)
600	Case 3	2.0024(0.008)	2.0086(0.005)	2.6155(0.4028)	2.0267(0.005)
1200	Case 4	2.0038(0.007)	2.0065(0.004)	2.7359(0.6534)	2.0246(0.004)

Table 1 presents RMSPE for the competing models, averaged over 100 replications, with standard errors provided in parentheses. Across varying values of J , the point prediction performance of XAI, BART, and GLM remains stable. XAI achieves comparable accuracy to BART and GLM, while significantly outperforming the deep learning alternative BIRD-GP. As shown in Figure 4, both XAI and BIRD-GP attain near-nominal coverage; however, XAI produces noticeably narrower predictive intervals. A closer inspection reveals that all four simulation scenarios assume a signal-to-noise ratio (SNR) below 1—reflective of the conditions in the real data application (Section 5)—with a sample size of $n = 300$. Due to its greater data requirements, BIRD-GP performs substantially worse than XAI under these settings, although the performance gap narrows as n and SNR increase. Meanwhile, BART severely underestimates uncertainty, yielding the narrowest predictive intervals and the lowest coverage among all competing methods.

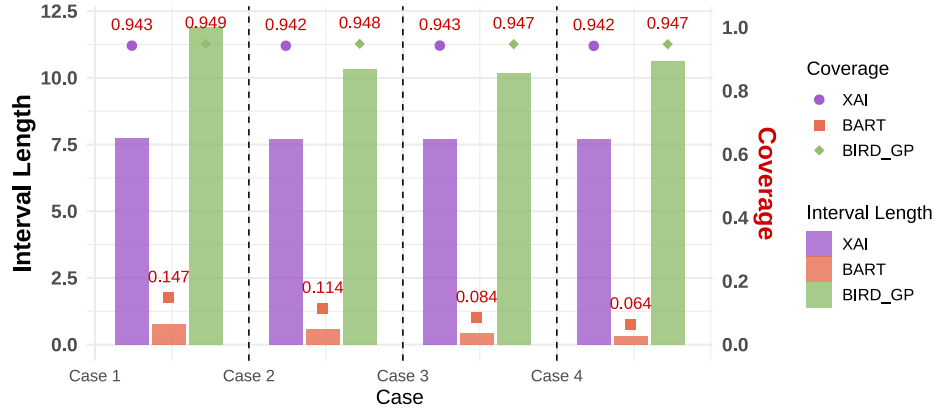


Figure 4: Coverage and length of 95% predictive intervals averaged over replications for XAI, BIRD-GP and BART. They are not available for GLM. Results show near nominal coverage of XAI with smaller predictive intervals than BIRD-GP.

4.3.2 Impact of Changing Signal-to-noise Ratios (SNRs)

To investigate the effect of SNRs, we design simulation scenarios by varying the variance parameters $\delta_{\beta_1}^2$, $\delta_{\beta_2}^2$ and δ_h^2 corresponding to the regression functions $\beta_1(\cdot)$, $\beta_2(\cdot)$, and $h(\cdot)$ while fixing the total number of ROIs at $J = 600$ and the number of nodes at $V = 30$. As shown in Table 2, increasing SNR corresponds to stronger spatial signals relative to noise.

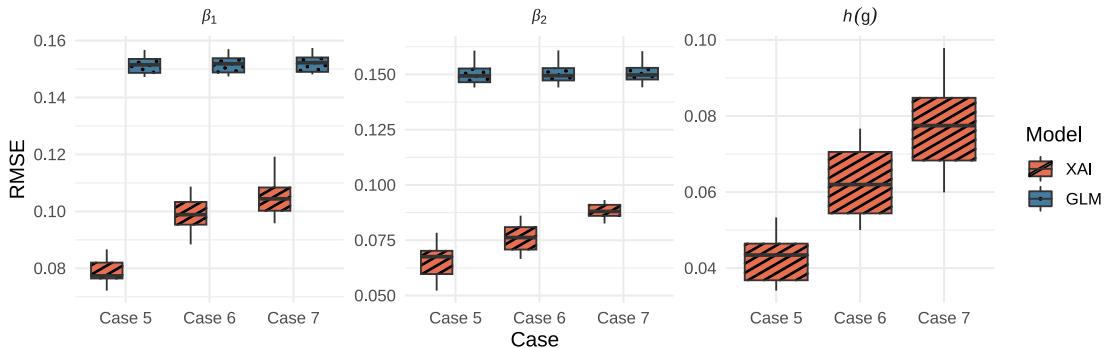


Figure 5: Root mean squared error (RMSE) comparison between the proposed XAI method and GLM for estimating the spatially varying coefficients $\beta_1(\mathbf{s})$ and $\beta_2(\mathbf{s})$, and the network latent effect $h(\mathbf{g})$ under Case 5 to Case 7. Boxplots show the distribution of RMSE across 100 simulation replications. The inference on $\beta_1(\mathbf{s})$, $\beta_2(\mathbf{s})$, $h(\mathbf{g})$ are not available for BART and BIRD-GP. The inference on $h(\mathbf{g})$ is not available for GLM.

Figure 5 highlights the superior performance of XAI over GLM in estimating the varying coefficients $\beta_1(\mathbf{s})$, $\beta_2(\mathbf{s})$ and the non-linear function encoding network latent effect $h(\mathbf{g})$.

Table 2: Prediction performance comparison for simulated datasets under Case 5 to Case 7 for varying signal-to-noise ratio (SNR), by varying the variance parameters $\delta_{\beta,1}^2, \delta_{\beta,2}^2, \delta_h^2$, while fixing the number of nodes (V) and the total number of ROIs (J). The table reports the root mean squared prediction error (RMSPE) with standard errors in parentheses for each method (XAI, BART, BIRD-GP and GLM). The standard errors are presented over 100 replications. Best performing model is boldfaced in each case.

$\delta_{\beta,1}^2$	$\delta_{\beta,2}^2$	δ_h^2	SNR	Cases	XAI	BART	BIRD-GP	GLM
2	1	1	0.42	Case 5	2.0020(0.009)	2.0080(0.005)	2.5549(0.382)	2.0267(0.005)
4	3	3	0.69	Case 6	2.0037(0.008)	2.0120(0.005)	2.9983(0.646)	2.0312(0.006)
5	6	5	0.81	Case 7	2.0052(0.008)	2.0155(0.005)	3.3656(0.782)	2.0358(0.008)

With changing SNR, GLM’s performance remains relatively unchanged, and the performance gap between GLM and XAI tends to get smaller with increasing SNR from Case 5 to 7. Since Cases 5–7 correspond to overall low SNR settings, XAI substantially outperforms its deep learning competitor BIRD-GP in terms of point prediction, as reflected in Table 2. Additionally, both BIRD-GP and XAI achieve near-nominal predictive coverage, although BIRD-GP produces credible intervals nearly twice as wide as those of XAI, as shown in Figure 6. BART provides comparable point prediction but severely underestimates uncertainty.

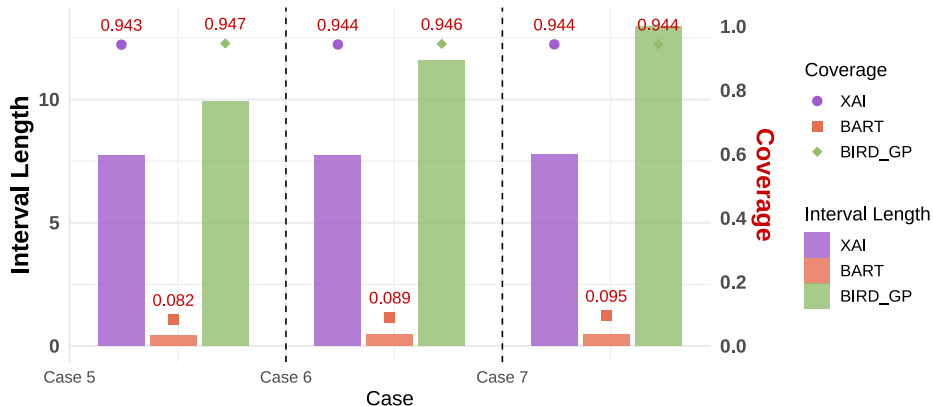


Figure 6: Coverage and length of 95% predictive intervals averaged over replications for XAI, BIRD-GP and BART. They are not available for GLM. Results show near nominal coverage of XAI with smaller predictive intervals than BIRD-GP.

Computation Time. In the XAI model, computation time primarily depends on sample size (n) and the total number of ROIs (J). To assess scalability, we fit XAI for $J = 100, 300, 500, 1000$ and $n = 300, 1000, 3000, 5000$, training each for 200 epochs with

batch size 64 and using MC dropout with $F = 200$ samples. As shown in Figure 7, computation time scales linearly with both n and J . For instance, full inference with $n = 5000$ and $J = 300$ takes under 5 minutes.

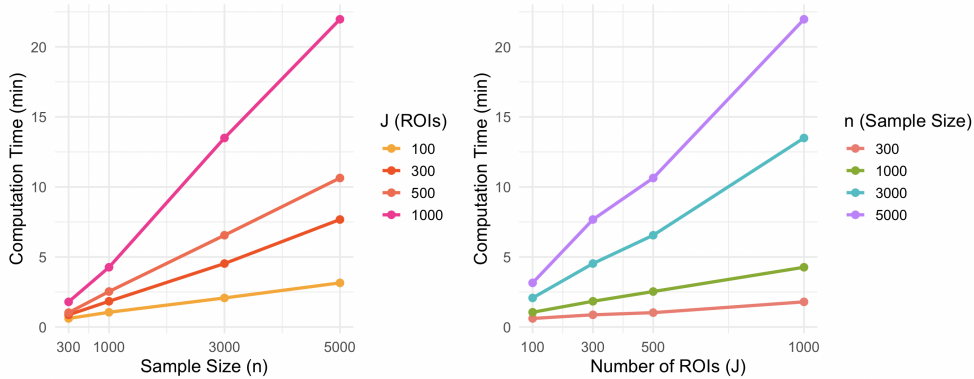


Figure 7: Computation time (in minutes) for XAI under varying dimensions of input data. Left: Computation time as a function of sample size n for different numbers of ROIs J . Right: Computation time as a function of the number of ROIs J for different sample size n .

5 Application to the Multimodal ABCD Data

5.1 Data Structure and Methods

We apply our proposed method to the ABCD dataset to answer our motivating scientific question described in Section 2. Each participant is observed with two structural images containing 148 ROIs and these ROIs are mapped to a 3-dimensional space using 3-dimensional coordinates obtained from the R package `brainGraph` [Watson, 2020]. Note that the raw outcome BOLDVAR contains some extreme values that fell well beyond the main density of the data. Therefore, we trimmed values greater than 3 which excluded most of these extreme values and resulted in missing data for 520 subjects yielding a total of 8655 subjects for the analysis data set. To facilitate interpretation of the targeted varying coefficient functions across ROIs, we scaled and centered both the log transformed outcome and local covariates within each ROI using the training data, such that they have a mean of zero and a standard deviation (SD) of one across subjects. This scaling yields standardized regression

coefficients that are directly comparable across ROIs allowing us to compare effects in terms of SD units. To incorporate the network structure into our model, we employ a latent space model described in Section 3.2.1, which generates 3-dimensional latent variables representing the network. For the network nodes, we define each node as a sub-group of ROIs organized based on similar anatomical location defined by hemisphere and lobe as described in Section 2. This hierarchical approach reduces the overall network complexity, allowing us to model the structure using only 12 nodes, despite the initial set containing 148 ROIs. This reduction in complexity is justified empirically based on preliminary analyses that considered co-activation networks among the full set of ROIs which produced comparable explanations of variation in the outcome but with much greater computational demands to perform the decomposition described in Section 3.2.1. Our analysis uses a total of $N = 5,193$ participants for model fitting, $N_{\text{val}} = 1,731$ participants for validation, and $N_{\text{test}} = 1,731$ participants for testing. We utilized validation data to find out the optimized tuning hyper-parameters such as batch size, learning rate, and number of layers. We compare our inferential performance with competitors in terms of R-squared (R^2) values computed as the proportion of variation explained for frequentist methods and as in Gelman et al. [2019] for Bayesian procedures. Here, the batch size is 30 with a maximum of 500 epochs, and, as mentioned in the simulation settings, we apply the same early-stopping rule and learning-rate scheduling based on the validation mean squared error. The BART and BIRD-GP models are also trained following the same configurations used in the simulation study.

5.2 Data Analysis Results

We present the results from our application of the proposed XAI model to the multimodal ABCD imaging data. Figure 8 displays lateral and medial cross sections of the posterior (a) mean and (b) 95% credible interval length for the spatially varying coefficient function $\beta_1(\mathbf{s}_{v,j})$ capturing effects of GWMIC. In Figure 8(a), positive (negative) regression coefficients can be interpreted as indicating a positive (negative) association between regions with greater cortical gray and white matter intensity contrasts and BOLDVAR. Figure 8(b)

shows the length of the 95% credible intervals (CI) for the estimated coefficient function, offering a measure of uncertainty—longer intervals reflect greater uncertainty, while shorter intervals indicate less uncertainty. When the posterior 95% credible interval contains zero, the interval length is marked with back stripes in the Figure 8(b). Roughly half of the 95% credible intervals for ROI-effects exclude zero (80/148 ROIs, 54.1%), where the greatest proportion of CIs excluding zero occurs in the insula (12/24 ROIs, 75.0%) and frontal (27/44 ROIs, 61.4%) suggesting these lobes are where our XAI model is most certain of an association between GWMIC and the outcome. Focusing on the coefficients with 95% CIs that exclude zero within each lobe, estimated effects range from -0.22 to 0.26 , indicating that within each ROI a SD increase in GWMIC is associated with generally less than a 0.26 SD shift in the outcome $\log(\text{BOLDVAR})$ reflecting a small standardized effect size. The estimated coefficient function shows a mixture of positive and negative associations within each lobe indicating a variable pattern of associations between GWMIC and BOLDVAR. Situating these results in relation to prior research, Zuo et al. [2010] found that gray matter in the brain displays higher ALFF than white matter, though these results focus on gray and white matter parcellations of the brain as opposed to cortical contrasts analyzed here. In fact, the relationship between BOLDVAR and GWMIC is essentially unexplored in adolescent children and these findings suggest a mixture of associations both within and across brain lobes when controlling for the contributions of CT and multi-task coactivation.

Figure 9 displays lateral and medial cross sections of the posterior (a) mean and (b) 95% credible interval length for the spatially varying coefficient function $\beta_2(\mathbf{s}_{v,j})$ capturing effects of CT. Figure 9(b), displays the 95% CI length for the estimated coefficient function and are interpreted as described above. Generally, 95% CIs for ROI-effects exclude zero (124/148 ROIs, 83.8%), suggesting our XAI model is relatively certain of the association between CT even in the occipital lobe (21/28 ROIs, 75.0%) which displays the greatest uncertainty of non-zero effects for CT. Focusing on the coefficients with 95% CIs that exclude zero within each lobe, estimated effects range from -0.38 to -0.05 , indicating that within each ROI a SD

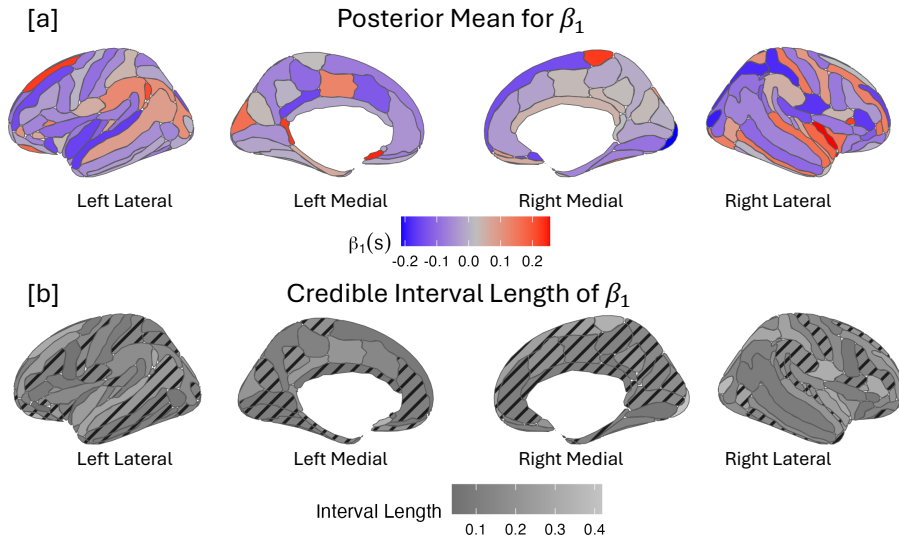


Figure 8: Lateral and medial cross sections of the posterior (a) mean and (b) 95% credible interval length for the spatially varying coefficient function $\beta_1(\mathbf{s}_{v,j})$ capturing effects of GWMIC. When the posterior 95% credible interval contains zero, the interval length is marked with back stripes in the figure as indication of uncertainty of any association.

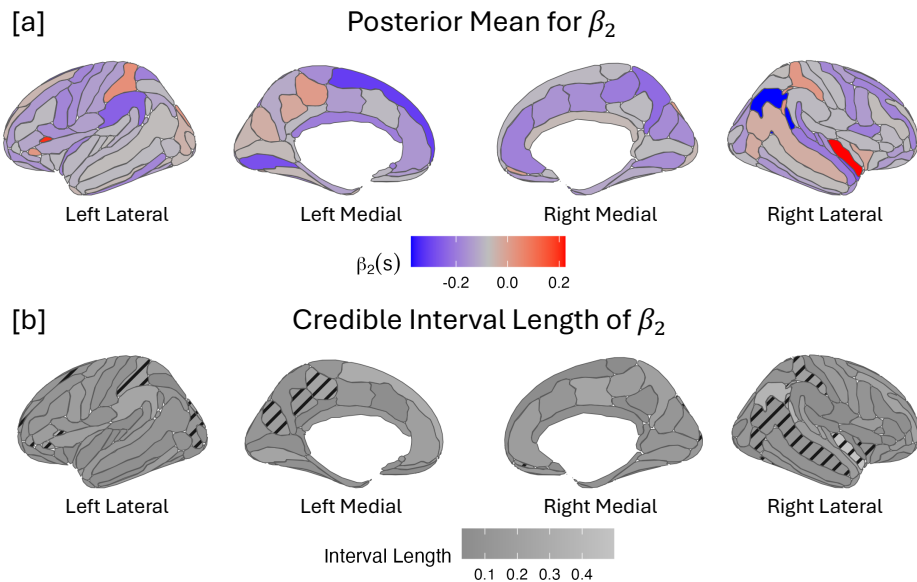


Figure 9: Lateral and medial cross sections of the posterior (a) mean and (b) 95% credible interval length for the spatially varying coefficient function $\beta_2(\mathbf{s}_{v,j})$ capturing effects of CT. When the posterior 95% credible interval contains zero, the interval length is marked with back stripes in the figure as indication of uncertainty of any association.

increase in CT is associated with up to a 0.38 SD decrease in the outcome $\log(\text{BOLDVAR})$ reflecting a small to medium standardized effect size. The estimated coefficient function

shows exclusively negative associations with the strongest signals in the temporal and limbic lobes. There is essentially no prior research on the relationship between BOLDVAR and CT in adolescent children and these results suggest a near uniform negative association throughout the brain that varies in magnitude from no effect to a medium effect size when controlling for the contributions of GWMIC and multi-task coactivation.

Table 3: Predictive inference results for real data application from different methods. For all methods, overall and average R^2 , prediction coverage, 95% HPD interval, and computing time (min) are reported in the table. †Frequentist R^2 is reported for the GLM models.

	XAI	BART	BIRD-GP	GLM
R-squared (overall)	0.029	-	0.011	0.026 †
Coverage	0.942	0.088	0.930	-
Intervals	3.804	0.222	3.627	-
Time (min)	29.763	130.421	170.745	0.125

Table 3 displays predictive performance and computational efficiency metrics for all methods, including R-squared, coverage, and interval width for our technique compared to the listed competitors. We report an overall R^2 computed by aggregating predictions across all ROIs without region-wise separation. In terms of our ABCD data, the R^2 suggests that our proposed XAI model explains the outcome image better than more complex models such as BIRD-GP, which allow for nonlinear interactions between imaging modalities. While BART and GLM cannot provide posterior predictive means and thus its Bayesian R^2 is not available. The frequentist R^2 for GLM is available and in the same range as our proposed method providing a qualitative comparison. As shown in Supplementary Figure 3, there is structural heterogeneity in R^2 performance, with some regions being well explained and others poorly captured, which demonstrates the region-specific differences among ROIs. Summarizing the results by lobe, the R^2 is highest in the temporal lobe followed by the frontal and occipital lobes, with the lowest predictive performance in the limbic lobe. We compare the R^2 for our XAI model with and without the network-valued inputs. Section 3 of the supplementary file shows a small improvement from compared to a model with spatial information alone.

Our proposed XAI model provides nominal coverage followed by BIRD-GP with near nominal coverage and BART with severe under coverage (see Table 3). In terms of credible interval length, BART provides the shortest intervals, explaining its poor coverage. In terms of computation, the XAI takes approximately four times less than other competitors that offer posterior predictive inference. In conclusion, XAI provides equivalent point prediction while yielding superior predictive uncertainties and much faster computation which are of critical importance when dealing with large neuroimaging data sets.

6 Conclusion

This article proposes a framework for estimating spatially-indexed spatially indexed low frequency fluctuations (ALFF) in resting state functional MRI as a function of cortical structural features and a multi-task coactivation network. The framework leverages deep neural networks to model complex nonlinear relationships between the input spatial and network-valued images and the spatial output image. It enables accurate estimation of the effect of each input image on the outcome image while providing crucial uncertainty quantification within DNN—both for prediction and for effect estimation—through a MC dropout strategy. In simulations and a real data analysis, the proposed explainable AI (XAI) approach demonstrates excellent performance in point estimation and uncertainty quantification. Additionally, the model scales linearly with the sample size and the number of brain regions, ensuring computational efficiency in high-resolution and large-scale neuroimaging studies.

While this article assumes a common relationship between the activation map, cortical metrics, and brain connectivity network across all subjects, an important direction for future work is to investigate how these relationships vary across individuals. This motivates the development of model-based clustering strategies, wherein the proposed XAI framework is fitted within each identified cluster. This extension is the focus of our ongoing research.

References

- Seyed Amir Hossein Batouli and Minoo Sisakhti. Some points to consider in a task-based fmri study: A guideline for beginners. *Frontiers in Biomedical Technologies*, 2020.
- Ingwer Borg and Patrick JF Groenen. *Modern multidimensional scaling: Theory and applications*. Springer Science & Business Media, 2005.
- B J Casey, Tariq Cannonier, May I Conley, Alexandra O Cohen, Deanna M Barch, and et al. The adolescent brain cognitive development (ABCD) study: Imaging acquisition across 21 sites. *Dev. Cogn. Neurosci.*, 32:43–54, 8 2018.
- Hugh A. Chipman, Edward I. George, and Robert E. McCulloch. Bart: Bayesian additive regression trees. *The Annals of Applied Statistics*, 4(1):266 – 298, 2010.
- Michael W Cole, Takuya Ito, Danielle S Bassett, and Douglas H Schultz. Activity flow over resting-state networks shapes cognitive task activations. *Nat. Neurosci.*, 19(12):1718–1726, 12 2016.
- Perry de Valpine, Daniel Turek, Christopher Paciorek, Cliff Anderson-Bergman, Duncan Temple Lang, and Ras Bodik. Programming with models: writing statistical algorithms for general model structures with nimble. *Journal of Computational and Graphical Statistics*, 26:403–413, 2017.
- Christophe Destrieux, Bruce Fischl, Anders Dale, and Eric Halgren. Automatic parcellation of human cortical gyri and sulci using standard anatomical nomenclature. *Neuroimage*, 53(1):1–15, 10 2010.
- Zening Fu, Yiheng Tu, Xin Di, Bharat B Biswal, Vince D Calhoun, and et al. Associations between functional connectivity dynamics and BOLD dynamics are heterogeneous across brain networks. *Front. Hum. Neurosci.*, 11:593, 12 2017.

- Yarin Gal and Zoubin Ghahramani. Bayesian convolutional neural networks with bernoulli approximate variational inference, 2016a.
- Yarin Gal and Zoubin Ghahramani. Dropout as a Bayesian approximation: Representing model uncertainty in deep learning. In *International Conference on Machine Learning*, pages 1050–1059. PMLR, 2016b.
- Alan E Gelfand, Hyon-Jung Kim, CF Sirmans, and Sudipto Banerjee. Spatial modeling with spatially varying coefficient processes. *Journal of the American Statistical Association*, 98(462):387–396, 2003.
- Andrew Gelman, Ben Goodrich, Jonah Gabry, and Aki Vehtari. R-squared for bayesian regression models. *The American Statistician*, 2019.
- Sharmistha Guha and Abel Rodriguez. Bayesian regression with undirected network predictors with an application to brain connectome data. *Journal of the American Statistical Association*, 116(534):581–593, 2021.
- Rajarshi Guhaniyogi, Cheng Li, Terrance D Savitsky, and Sanvesh Srivastava. Distributed bayesian varying coefficient modeling using a gaussian process prior. *Journal of machine learning research*, 23(84):1–59, 2022.
- Donald J Hagler Jr, SeanN Hatton, M Daniela Cornejo, Carolina Makowski, Damien A Fair, et al. Image processing and analysis methods for the adolescent brain cognitive development study. *Neuroimage*, 202:116091, 2019.
- Yeseul Jeon, Won Chang, Seonghyun Jeong, Sanghoon Han, and Jaewoo Park. A bayesian convolutional neural network-based generalized linear model. *Biometrics*, 80(2), 2024.
- Charlie Kirkwood, Theo Economou, Nicolas Pugeault, and Henry Odbert. Bayesian deep learning for spatial interpolation in the presence of auxiliary information. *Mathematical Geosciences*, 54(3):507–531, 2022.

- Kexuan Li, Jun Zhu, Anthony R Ives, Volker C Radeloff, and Fangfang Wang. Semiparametric regression for spatial data via deep learning. *Spatial Statistics*, 57:100777, 2023.
- Guoxuan Ma, Bangyao Zhao, Hasan Abu-Amara, and Jian Kang. Bayesian image-on-image regression via deep kernel learning based gaussian processes. *arXiv:2311.05649*, 2023.
- Jorge Mateu and Abdollah Jalilian. Spatial point processes and neural networks: A convenient couple. *Spatial Statistics*, 50:100644, 2022.
- Jeffrey S Morris. Functional regression. *Annual Review of Statistics and Its Application*, 2(1):321–359, 2015.
- Eric W Prince, Debashis Ghosh, Carsten Görg, and Todd C Hankinson. Uncertainty-aware deep learning classification of adamantinomatous craniopharyngioma from preoperative mri. *Diagnostics*, 13(6):1132, 2023.
- Muhammad Imran Razzak, Saeeda Naz, and Ahmad Zaib. Deep learning for medical image processing: Overview, challenges and the future. *Classification in BioApps: Automation of decision making*, pages 323–350, 2018.
- Philip T Reiss, Jeff Goldsmith, Han Lin Shang, and R Todd Ogden. Methods for scalar-on-function regression. *International Statistical Review*, 85(2):228–249, 2017.
- Jintao Sheng, Liang Zhang, Junjiao Feng, Jing Liu, Anqi Li, and et al. The coupling of BOLD signal variability and degree centrality underlies cognitive functions and psychiatric diseases. *Neuroimage*, 237:118187, 8 2021.
- Jing Sui, Tülay Adalı, Qingbao Yu, Jiayu Chen, and Vince D Calhoun. A review of multivariate methods for multimodal fusion of brain imaging data. *J. Neurosci. Methods*, 204(1):68–81, 2 2012.

- D Tomasi, E Shokri-Kojori, and N D Volkow. Temporal changes in local functional connectivity density reflect the temporal variability of the amplitude of low frequency fluctuations in gray matter. *PLoS One*, 11(4):e0154407, 4 2016.
- Dardo Tomasi and Nora D Volkow. Association between brain activation and functional connectivity. *Cereb. Cortex*, 29(5):1984–1996, 5 2019.
- Masayuki Tsuneki. Deep learning models in medical image analysis. *Journal of Oral Biosciences*, 64(3):312–320, 2022.
- Hongye Wang, Amirhossein Ghaderi, Xiangyu Long, Jess E Reynolds, Catherine Lebel, and Andrea B Protzner. The longitudinal relationship between BOLD signal variability changes and white matter maturation during early childhood. *Neuroimage*, 242:118448, 11 2021.
- Christopher G. Watson. braingraph: Graph theory analysis of brain mri data, 2020. URL <https://CRAN.R-project.org/package=brainGraph>.
- Christopher K Wikle and Andrew Zammit-Mangion. Statistical deep learning for spatial and spatiotemporal data. *Annual Review of Statistics and Its Application*, 10(1):247–270, 2023.
- Fengdan Ye, Robert Kohler, Bianca Serio, Sarah Lichenstein, and Sarah W Yip. Task-based co-activation patterns reliably predict resting state canonical network engagement during development. *Dev. Cogn. Neurosci.*, 58(101160), 12 2022.
- Andrew Zammit-Mangion, Michael D Kaminski, Ba-Hien Tran, Maurizio Filippone, and Noel Cressie. Spatial bayesian neural networks. *arXiv preprint arXiv:2311.09491*, 2023.
- Jianfeng Zhang, Dong-Qiang Liu, Shufang Qian, Xiujuan Qu, Peiwen Zhang, and et al. The neural correlates of amplitude of low-frequency fluctuation: a multimodal resting-state MEG and fMRI-EEG study. *Cereb. Cortex*, 33(4):1119–1129, 2 2023.

Ke Zou, Zhihao Chen, Xuedong Yuan, Xiaojing Shen, Meng Wang, and et al. A review of uncertainty estimation and its application in medical imaging. *Meta-Radiology*, page 100003, 2023.

Xi-Nian Zuo, Adriana Di Martino, Clare Kelly, Zarrar E Shehzad, Dylan G Gee, and et al. The oscillating brain: complex and reliable. *Neuroimage*, 49(2):1432–1445, 1 2010.